Pharm Res (2011) 28:572–584
DOI 10.1007/s11095-010-0306-4

RESEARCH PAPER

Atomic Force Microscopy-Based Screening of Drug-Excipient Miscibility and Stability of Solid Dispersions

Matthias Eckhard Lauer • Olaf Grassmann • Monira Siam • Joseph Tardio • Laurence Jacob • Susanne Page • Johannes Heinrich Kindt • Andreas Engel • Jochem Alsenz

Received: 8 July 2010 / Accepted: 13 October 2010 / Published online: 3 November 2010

ABSTRACT

Purpose Development of a method to assess the drug/polymer miscibility and stability of solid dispersions using a melt-based mixing method.

Methods Amorphous fractured films are prepared and characterized with Raman Microscopy in combination with Atomic Force Microscopy to discriminate between homogeneously and heterogeneously mixed drug/polymer combinations. The homogenous combinations are analyzed further for physical stability under stress conditions, such as increased humidity or temperature.

Results Combinations that have the potential to form a molecular disperse mixture are identified. Their potential to phase separate is determined through imaging at molecular length scales, which results in short observation time. De-mixing is quantified by phase separation analysis, and the drug/polymer combinations are ranked to identify the most stable combinations.

Conclusions The presented results demonstrate that drug/polymer miscibility and stability of solid dispersions, with many mechanistic details, can be analyzed with Atomic Force Microscopy. The assay allows to identify well-miscible and stable combinations within hours or a few days.

KEY WORDS amorphous formulation · raman microscopy · solid dispersion · stability prediction · AFM

ABBREVIATIONS

AFM	atomic force microscopy
API	active pharmaceutical ingredient
CETP2	CETP inhibitor (2)
Eudragit L100	polymethacrylate
HME	hot-melt extrusion
HPMCAS MF	hydroxypropyl methylcellulose acetate succinate
NK1(1)	NK1 antagonist (1)
PVP K30	polyvinylpyrrolidone K30
PVP17PF	polyvinylpyrrolidone 17PF
PVP VA 64	copolymer of 1-vinyl-2-pyrrolidone and vinyl acetate
RH	relative humidity
SEM	scanning electron microscopy
T	temperature
TEM	transmission electron microscopy

Electronic Supplementary Material The online version of this article (doi:10.1007/s11095-010-0306-4) contains supplementary material, which is available to authorized users.

M. E. Lauer (✉) · A. Engel
Center for Cellular Imaging and Nanoanalytics, Biozentrum
University of Basel
Mattenstrasse 26
CH 4006 Basel, Switzerland
e-mail: Matthias.Lauer@roche.com

M. E. Lauer · O. Grassmann · M. Siam
F. Hoffmann-La Roche Ltd., Discovery Technologies
CH-4070 Basel, Switzerland

J. Tardio · L. Jacob · S. Page · J. Alsenz
F. Hoffmann-La Roche Ltd., Formulation Research
CH-4070 Basel, Switzerland

J. H. Kindt
Bruker Nano GmbH
Dynamostrasse 19
68165 Mannheim, Germany

INTRODUCTION

A most frequently used option to improve the oral bioavailability of poorly water-soluble drugs with high melting points is to prepare an amorphous solid dispersion. This can be achieved by a number of techniques, such as micro-precipitation, ball milling, or hot-melt extrusion (HME). The amorphous drug gets thereby dispersed and stabilized within a polymer matrix, and a binary amorphous mixture is generated. Amorphous formulations can show higher drug dissolution rates, since the crystal lattice energy is no longer a barrier for the required dissolution step. A general disadvantage of this approach is that a solid dispersion can be unstable and that the drug can crystallize with time. The study of drug/polymer miscibility and the knowledge about how given environmental factors such as temperature and/or humidity trigger these processes are crucial. Therefore, time-consuming stress tests need to be carried out to identify appropriate formulations with sufficient shelf life.

The production and long-term stability of homogenous binary amorphous mixtures is an important topic in various fields of academic and industrial research. The physicochemical analogies and differences with the formulation of polymer blends were recently reviewed, and the importance for pharmaceutical scientists to rationally assess solubility and miscibility in order to select the optimal formulation was highlighted (1). The thermodynamic models, which are usually based on the theory of Flory and Huggins, principally allow for describing the phase behavior of a polymer within a given solvent, or alternatively within a melt of small molecules, or within another polymer (2,3). These theories are also the common base to model phase separations (4) and are applied to predict and calculate the stability of solid drug dispersions (5). Therefore, it is well-known that the solubility and miscibility strongly drops with the length of the polymer chain, the polymer weight of a molecule for entropic reasons. When a binary melt mixture, however, of principle non-miscible compounds is heated to above their critical temperature (T_c), the entropy term starts to overcompensate the positive free energy of mixing. The consequence is that even a low-solubilty polymer can principally be dispersed within the melt, and at all possible ratios. Deep quench cooling of such mixtures from above to much below T_c is therefore a way to create a homogenous and glassy solid dispersion. Quench-cooled melt mixtures are therefore used to screen whether a drug molecule has the intrinsic (intrinsic in this context means a process independent) potential to form a homogenous glass at a given temperature, or maybe not (6). The drug/polymer solubility, or miscibility, is crucial, because it impacts the results and success of, for example, a hot-melt extrusion approach from a general point of view. Miniaturized prescreens are in this and comparable contexts already established for hot-melt extrusions or even spray drying, since they are likewise material- and resource-intensive processes (7,8). Solvent cast films are commonly used to gather early information on drug miscibility and stabilization and were in various contexts already helpful to define and predict the requirements of final formulations (9). However, even a glassy homogenous dispersion can be supersaturated and will then always have the potential to undergo phase separation over time (10,11) and, as reviewed recently, even below the phase transition temperature (12) or accelerated when exposed to moisture (13,14). Many solid dispersions, however, were shown to have a sufficient kinetic stability, which practically prevents them from solid-state de-mixing, and/or to reach their origin thermodynamic equilibrium within a critical time frame (15). In this context, it is helpful to quickly identify the excipient, mixing ratios, and mixing temperature, where the finally achieved kinetic material stability and/or the chemical potential to de-mix is well or acceptably balanced. Different approach principles allow this (16).

As experimentally noticed and theoretically expected, drug crystallizations are likely to be triggered by phase separations (17). The growth rate of separating phases in solid and liquid mixtures can be directly measured, screened, modeled and quantified (18,19). A broad analytical toolbox is established to monitor this process. When the materials are initially molecularly disperse and the phase growth occurs slowly, with velocities in the range of v~nm/hr, high-resolution imaging technologies like Transmission Electron Microscopy (TEM), Scanning Electron Microscopy (SEM) or Atomic Force Microscopy (AFM) are probably suitable (20). They allow for studying phase separation directly and on molecular length scales, which results in much shorter observation times. The capability of AFM to study de-mixing mechanisms over time and in the presence of various environmental factors was already demonstrated on solid drug dispersions (21), polymer blends (22), glass (23), food (24), and probably many other materials. Because the samples can also be fractured, or sectioned with a microtome, bulk and surface evolution can accurately be differentiated (25,26). This is relevant because humidity-driven phase separations are thought to be surface directed (27).

First studies in the field of amorphous pharmaceutical formulations with AFM were carried out already a decade ago, and since then a number of other studies were published. The focus of these studies is on the growth rates of drug single crystals within different excipient combinations (28–32). The capability of AFM to identify nanometer-sized grains was recently demonstrated, utilizing a new scanning technique: Carbamapezine particles measuring ~50 nm in diameter were first mapped by AFM imaging and, in a second step, studied with regard to their melting properties under constant force (33). Nanoindentation testing on crystallized drug particles, for example, can also be used to identify and discriminate between different polymorphs (34); AFM and other applications in this field are topic of review articles (35,36).

The published results in this and the other areas initiated the development of a miniaturized assay to measure/compare the nanometer homogeneity of various solid dispersions on the molecular scale and to analyze their solid state stability and their potential to undergo phase separations in humid environment on micrometer and nanometer length scales. In order to develop a miniaturized screening assay that can reflect the miscibility and stability of a drug within various polymers, a uniform, widely applicable, robust, easy to apply, and reproducible preparation procedure and workflow needed to be established. We here report the developed protocol and workflow and demonstrate the analytical potential on two different APIs.

MATERIALS AND METHODS

Compound Selection

The selection of Active Pharmaceutical Ingredients (APIs) and excipients was based on experimental results from previous unpublished projects. A CETP Inhibitor (2), which will be referenced CETP(2) (37), and a NK1 Receptor Antagonist (38), which will be referenced NK1(1), were selected. CETP(2) has a melting point (T_m) of $T_\mathrm{m}=142°\mathrm{C}$, and that of NK1(1) is $T_\mathrm{m}=130°\mathrm{C}$. The latter material, NK1(1), has a likewise higher tendency to crystallize and was known to be more difficult to stabilize than CETP(2). The excipient selection focused on the polymer class, and five different polymers were chosen: Copolymer of 1-vinyl-2-pyrrolidone and vinyl acetate (PVP VA 64, BASF, Ludwigshafen, Germany), Polyvinylpyrrolidone K30 (PVP K30, BASF, Ludwigshafen, Germany), Polyvinylpyrrolidone 17PF (PVP17PF, BASF, Ludwigshafen, Germany), Hyrdroxypropyl methylcellulose acetate succinate (HPMCAS MF, Shin-Etsu, Tokyo, Japan), Polymethacrylate (Eudragit L100, Roehm GmbH & Co. KG, Darmstadt, Germany).

Preparation of Deep-Quench-Cooled Melt Mixtures (DQCMM)

Glassy API/excipient (1:1) films were first generated by solvent casting: approximately 20 mg of prepared physical powder mixtures were dissolved in 2 ml acetone/methanol (1:1) and stirred at room temperature. Clear solutions were obtained. One-hundred microliters of each solution were deposited drop-wise on well-cleaned pre-heated optical glass slides ($T\sim 70°\mathrm{C}$), which is ~20°C above the solvent boiling point. Optically transparent films, glassy states, with thicknesses in the range of hundred(s) of micrometers, were obtained for all mixtures after the solvent was thermally evaporated. The films were heated to 180°C, which is ~40°C higher than the melting point of the APIs to be studied. The liquid mixtures were allowed to thermally equilibrate for one minute before being covered with a well-cleaned second glass slide pre-heated to 180°C. Top slides were pressed down using finger forces to better homogenize and distribute the viscous liquids, the co-melts, sandwiched between the slides. The sandwiched samples were placed on a smooth steel block at room temperature and cooled within minutes. For the AFM investigations, film fracture surfaces were generated by pushing a razor blade between the glass slides to crack, but not to cut, the cooled glasses apart. Care was taken not to investigate a film/glass interface, bubble regions, or a defect. For stability tests, surface de-mixing was studied on freshly fractured samples, which were stored in an open petri dish and exposed to stress conditions: accelerated stability conditions ($T=45°\mathrm{C}$, $\mathrm{RH}=75\%$). The samples were removed from the humid, high-temperature environment and immediately dried within a vacuum chamber. Phase separations within the bulk were studied by stressing freshly prepared samples still sandwiched between the glass slides. The DQCMMs were stored for an additional 96 h at $T=80°\mathrm{C}$ before being fractured and analyzed as described above.

Raman Microscopy

Raman mapping experiments were performed on a LabRAM ARAMIS (HoribaJobinYvon) Raman microscope equipped with a Peltier cooled CCD detector using laser excitation at 785 nm and a 600 1/mm grating centered at 1000 cm^{-1} (wave number range 320–1600 cm^{-1}). For each sample, at least 169 (13×13) spectra were recorded in an area of $240\times240\ \mu\mathrm{m}^2$ using a 50× objective (Olympus, NA 0.75). Settings were chosen to guarantee a spatial resolution of at least 20 μm (size of measurement spot for a single Raman spectrum). All Raman spectra of one mapping experiment were evaluated by integration of bands typical for API or excipient in the mixture. Homogeneity was judged by the ratio variation of API and excipient.

Atomic Force Microscopy

Fractured films on microscopic glass slides were directly mounted on the micrometer positioning stage of the Dimension V AFM (Veeco Instruments/Bruker). Between 5 and 25 regions per sample were automatically characterized using the software routine "programmed move" in the

Tapping Mode (Veeco Nansocope V7 r21). Height, phase, and amplitude images were collected simultaneously, using etched silicon cantilevers with a nominal spring constant of $k = 3.0$ N/m (Veeco Probes, RFESP), or alternatively of $k =$ 20–80 N/m (Veeco Probes, RTESPA). The typical free vibration amplitude was in the range of $A = 25$ nm; the images were recorded with set-point amplitudes corresponding to 60–70%. Image areas of 3×3 μm^2 were recorded at a resolution of 1024×1024 pixels. All data were automatically plane-corrected before analysis. Molecular fracture roughness data as displayed in Figs. 3 and 8 show the root mean square roughness and standard deviation calculated from at least 10 images collected on different regions and on each sample, using Scanning Probe Image Processor (SPIP 5.0.1, Image Metrology). Threshold masks were fit to detected phases and patterns, as explicitly shown in Fig. 5. Such distinct features were then defined as discrete single particles. SPIP software equipped with the module "particle and pore analysis" was used to determine the nearest neighbor distance distributions of those particles. The averaged particle separation distance, which is also a measure of the pattern periodicity, is shown and used to compare the differently sized spacing of the detected spinodal separation patterns.

RESULTS

Homogeneity

Figure 1 shows the chemical structure of the APIs, NK1(1) and CETP(2), which were selected to be profiled with regard to their chemical miscibility within a set of five different excipients (PVP VA 64, PVP K30, HPMCAS MF, PVP 17 PF, Eudragit L100) at $T = 180°C$. Dissolved material (1:1) was deposited on pre-heated optical glass slides, followed by annealing to desired temperature of, in this case, $T = 180°C$. After quench cooling and creation of a fracture surface, the films were characterized with optical microscopy and Raman microscopy with respect to their optical homogeneity and their spectroscopic uniformity on the micrometer scale. The results are summarized in Table 1.

The films, which are judged to be homogenous on the micrometer range (Table 1), fulfill two chosen pre-selection criteria: i) The API and excipient distributions visualized in the Raman maps are similar/comparable, but not complementary. ii) The overall API or excipient contrast scales with the variations also present in the additionally collected optical micrograph. This is in detail shown for a homogenous and for a non-homogenous case within Fig. 2. The optical micrograph in Fig. 2a shows the dimensions of a so-called hackle region and was recorded on the NK1(1) combination with PVP K 30. Comparable morphologies characterize the NK1(1) and CETP(2) combinations with PVP VA 64, PVP PF 17, PVP K 30, and HPMCAS MF, and are typically observed on fractured glasses (39) or polymer blends (40). The non-homogenous combination constituted from NK1(1) with Eudragit L100 is shown in Fig. 2b for comparison. The corresponding Raman maps are shown in the corners of the optical micrographs and were gathered on 240×240 μm^2-sized regions localized as illustrated in the center of the micrographs with the blue-colored point masks. Every point of the map corresponds to a discrete location chosen to collect a local Raman spectrum. From these locally recorded spectra, intensity maps were created by integration of a Raman band specific for the API or the polymer, respectively. Because intensity scales with the locally detected concentration, the distribution for the API (NK1(1) or CETP(2)) and the excipient can be visualized in form of a pixel map (red and black for NK1 (1), blue and black for PVP K30, green and black for Eudragit L100). The pixel maps visualize the local amount of detected NK1(1) and excipient, respectively. In the homogenous case (Fig. 2a), a comparable distribution of black pixels in the NK1(1) map (red) and the excipient map (blue) are found. Generally, the contrast scales with the morphological features resolved in the optical micrograph of Fig. 2a. Such samples were judged to be homogenous at the micrometer scale.

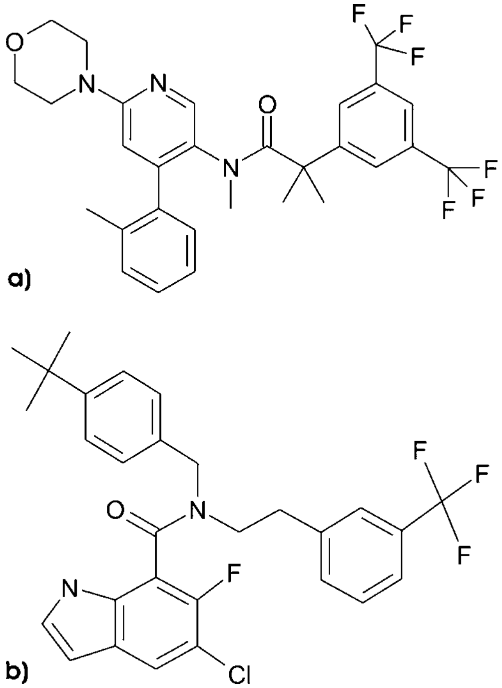

Fig. 1 Chemical structure of selected APIs. **a** NK1 receptor antagonist, and **b** CETP inhibitor.

The NK1(1): Eudragit L100 film, however, which is the only combination in our experiments judged to be non-homogenous, is in two ways different (Fig. 2b). The

Table I Micrometer Homogeneity of Profiled API/Excipient Mixtures

	PVP VA 64	PVP K 30	HPMCAS MF	PVP PF 17	Eudragit L 100
NK1(1)	homogenous	homogenous	homogenous	homogenous	heterogenous
CETP(2)	homogenous	homogenous	homogenous	homogenous	homogenous

homogenous/heterogenous: spectroscopically/microscopically uniform/non-uniform distribute on of API/excipient

red-colored NK1(1) map has discrete regions, which are in respect to their pixel intensity complementary to those noticeable in the excipient map. Two such regions were directly marked just for illustration. As can be seen by comparing the Raman maps with the corresponding optical micrograph, this complementary contrast is not due to variations in the sample morphology, even when the applied point mask or spatial resolution suffices to completely resolve the fractal features visible in the optical micrograph. Thus, both selection criteria are not fulfilled. First, the API excipient distribution is heterogeneous. Second, the variations cannot be explained with variations in the morphology. Thus, the composition NK1(1)–Eudragit L100 is heterogeneous on the micrometer scale.

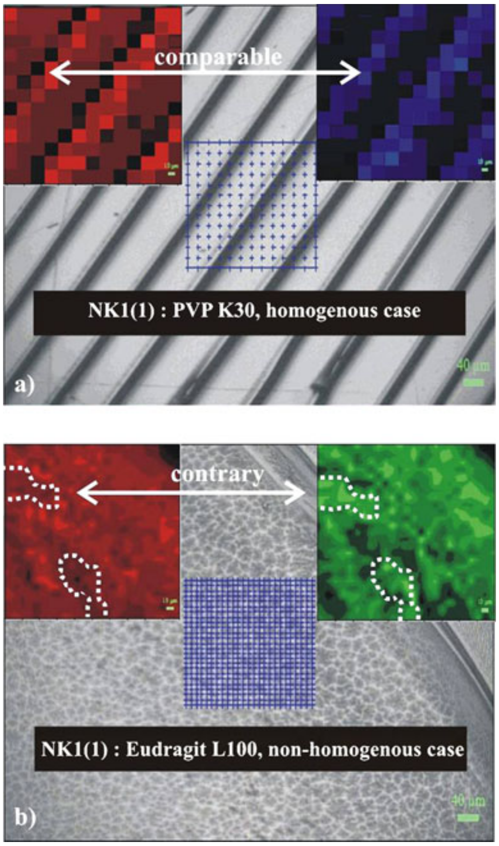

Fig. 2 Optical micrographs and Raman maps show data of a homogenous combination, NK1(1):PVP K 30 (**a**), and of a non-homogenous combination NK1(1) : Eudragit (**b**). The Raman contrast maps in the corners show local variation of NK1(1) amount with a black-red contrast, and that of the applied excipient with a black-blue contrast for PVP K 30, and a black-green contrast for Eudragit L100. Black regions have a low amount of NK1(1) or PVP K30/Eudragit L100; intense colors indicate material rich sample regions.

All fractured films were then analyzed by Atomic Force Microscopy with respect to their molecular homogeneity; the results are summarized in the Table 2. Combinations thereby judged homogenous at the nanometer scale fulfill two additional criteria: i) Ten different regions on each combination were analyzed with respect to their molecular fracture roughness and with respect to the roughness variations of the different sample regions. A homogenous film combination has to have a roughness, and a variation of roughness not significantly bigger than on the corresponding excipient blank (Fig. 3b). ii) The surface contact properties as visualized by phase maps with tapping mode AFM need to scale only with molecular morphological variations or fracture roughness. This means that a fracture surface was not picked if it exhibits islands, droplets, and domains with distinct mechanical property contrast, because such surfaces were related to separated, and nanometers-sized phases, clearly larger than a single polymer molecule (Fig. 4).

The bar diagrams in Fig. 3b show the root mean square roughness and the standard deviation of all investigated combinations. The morphologies of the 15 different sample surfaces are qualitatively comparable, because they are all characterized by molecular morphologies with size dimensions typical for single polymer molecules, or particles, which have an average diameter in the range of 10 nm. A typical fracture morphology is explicitly shown for the NK1 (1) combination with PVP VA 64 with a 3×3 μm^2–sized height image in Fig. 3a, with the overall color contrast corresponding to 20 nm. Significant differences between the differently constituted, but overall morphologically comparable, fracture surfaces are apparent when the fracture surfaces are analyzed and compared quantitatively. The investigated combinations and also the blank excipients are found to have specific size ranges with regard to their fracture roughness or their molecular morphologies. HPMCAS MF, for example, fractures rougher than films with PVP K30. A surprising trend appears to be that the fracture roughness and roughness variations of the micrometer homogenous NK1(1) combinations can be quantitatively compared with that of micrometer homogenous CETP(2) combinations, except for the combination with

Table II Nanometer Homogeneity of Profiled API/Excipient Mixtures

	PVP VA 64	PVP K 30	HPMCAS MF	PVP PF 17	Eudragit L 100
NK1(1)	homogenous	homogenous	homogenous	homogenous	heterogenous
CETP(2)	homogenous	homogenous	homogenous	homogenous	heterogenous

homogenous: no separated phases detected with AFM; heterogenous: separated phases observed with AFM

Eudragit L100. In the homogenous cases, the API molecules are found to have a smoothing effect on the fracture surface, as can be found by comparing the roughness diagrams of the combinations with the corresponding excipient blanks. The morphological surface variations, as quantified by the standard deviations, on PVP VA 64 and PVP K30 samples are found to be generally smaller than on HPMCAS MF or PVP 17PF. The API combinations with Eudragit L100, however, are found to be significantly different. The roughness variations in these combinations are much bigger, and the smoothing effect is missing. The additionally recorded phase maps complementarily show that the smooth and homogenously fractured film combinations have a molecularly homogenous contrast (Fig. 4). In these cases, the contrast detected only scales with the molecular morphological variations, the sample landscape variations, or surface roughness. Discrete islands, droplets, or domains, which behave mechanically or structurally different from the background, are not observed. Thus, these combinations are found to be molecularly homogenous on the nanometer scale. The combinations with Eudragit L100 are in two ways different: First, these combinations fracture likewise heterogeneously; second, the phase maps directly show discrete features in form of discrete particles comprised of ~80 nm-sized aggregates (Fig. 4j) or worm-like structures (Fig. 4o). The nanometer homogeneity criteria are not fulfilled, and the Eudragit L100 combinations were therefore discarded from the subsequent stability studies.

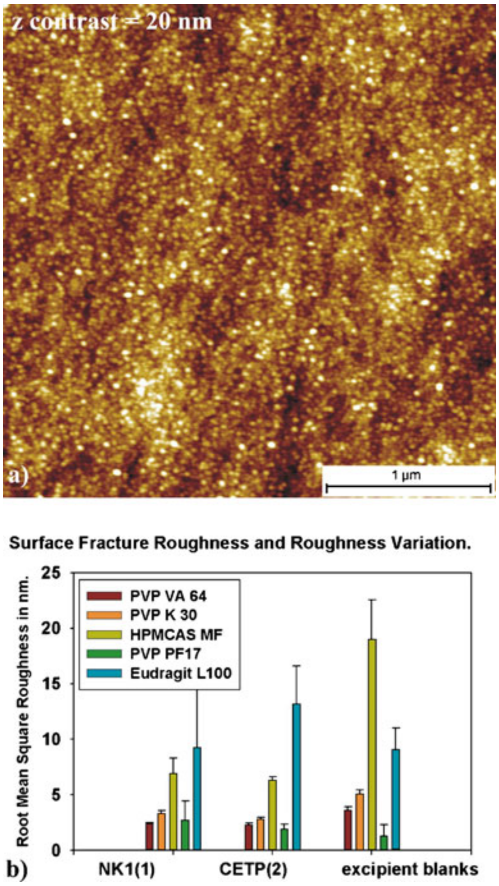

Fig. 3 Fracture Morphology and Root Mean Square roughness of the profiled API/excipient combinations and the excipient blanks. **a** $3\times3\ \mu m^2$ size height image as recorded on fracture surface of NK1(1)/PVP VA (1:1) film, **b** Root Mean Square Roughness and standard deviations of the different combinations and corresponding excipient blanks.

Surface Potential to De-mix Under Accelerated Stability Storage

Freshly fractured film combinations, which are found to be homogenous/miscible on the micrometer/nanometer scales (Table 1, Figs. 2, 3 and 4), were exposed for 2 h to stress conditions (T=40°C, RH=75%). After stress storage, 10 independent regions per sample were re-investigated using tapping mode AFM. The phase maps are shown in Fig. 5 and can directly be compared with the data recorded on non-stressed samples shown in the Fig. 4. The phase maps recorded on films after stress storage (Fig. 5) reveal discrete features that are absent on non-stressed materials (Fig. 4). It is evident that all combinations de-mix under stress conditions. Similar features can be observed on non-pharmaceutical materials as well and are due to nanometer-scale phase separations (26). On the NK1(1) combinations, spinodal de-mixing patterns with separation distances and pattern periodicities on the nanometer scale are typical (Fig. 5a–d). In contrast, the CETP(2) combinations show islands, droplets, or domains, which more independently seem to decorate the surface (Fig. 5e–h). To identify the relatively most-stable mixture, it is necessary to

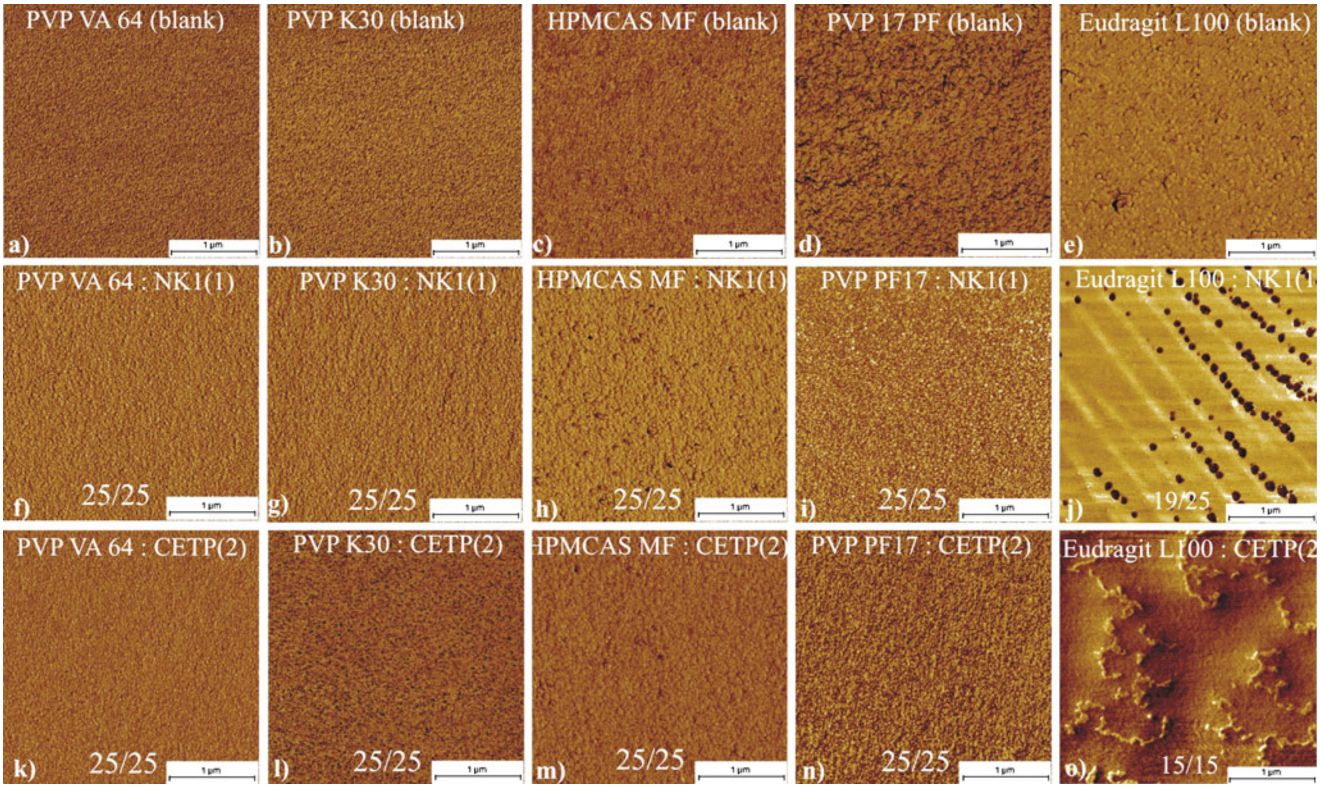

Fig. 4 Nanometer homogeneity is shown with phase maps recorded with tapping-mode AFM on fracture surfaces of the blank excipients (**a**–**e**), and corresponding combinations with NK1(1) (**f**–**j**), and with CETP(2) at the bottom (**k**–**o**). The numbers visible in the image rows (**f**–**j**, and **k**–**o**) relate the number of comparably structured places with the number of investigated places. The scale bars as shown throughout all images are the same and correspond to a length of 1 μm.

compare these details and differences. The patterns typical for the NK1(1) combinations indicate a spinodal separation process. The patterns can be compared by their periodicity, as it is performed on polymer blends and other materials (25). The features evolved on CETP(2) combinations indicate a nucleation and growth mechanism. The most stable material is that on which the relative surface coverage with features is minimal (41). The applied concepts are

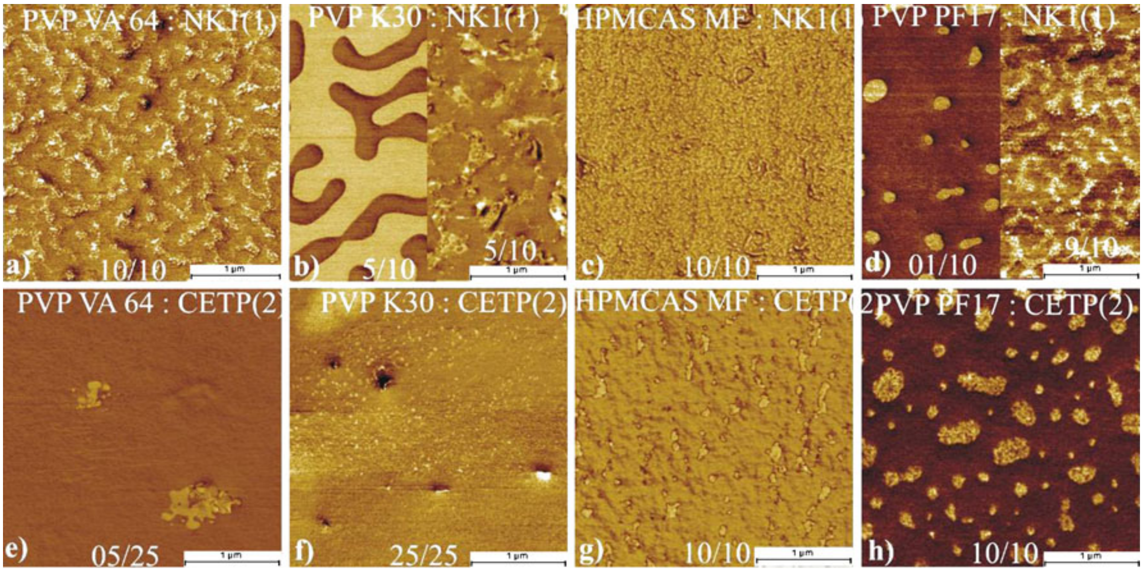

Fig. 5 Phase maps recorded with tapping mode AFM on miscible NK1(1):excipient combinations (**a**–**d**), and on corresponding CETP(2) combinations (**e**–**h**) after exposure to stress conditions (RH = 75%, T = 40°C) for 2 h. The initial and homogenous states are shown in Fig. 4 for comparison. The numbers visible in the images relate the amount of comparably structured places with the amount of investigated places. The scale bars as shown throughout all images are the same and correspond to a length of 1 μm.

demonstrated in detail as follows. Figure 6a shows two phase maps which were recorded with tapping-mode AFM. The maps were collected on an NK1(1) : PVP VA 64 combination, which had been exposed to similar stress conditions (T=40°C, RH=75%), but for different times. The upper and red-coded image is a surface state recorded after ~2 h exposure; the bottom image is typical for a ~12 h treatment. Both maps are patterned with distinct features; the separated phases are marked with intense colors for illustration. The colored regions obviously differ with respect to their average size, but also with respect to their relative spacing. In an early stage, spinodal patterns are narrow, but over time, and depending on the surface convection and thermal flux, they ripen with regard to their separation and size (42). The two histograms (Fig. 6a) show the nearest neighbor distribution and quantitatively express the different pattern periodicities, which are typical for the different states. It is evident that the spacing of evolving phases generally increases over time. The different patterns which were found to be characteristic for the four different NK1(1) films, as shown in Figs. 5a–d, were analyzed in the same manner. The determined averaged nearest neighbor distance for each combination is illustrated in Fig. 6b. Therefore, the separation length on the HPMCAS MF combination is shorter than that on PVP VA 64, PVP PF 17, or PVP K 30 combinations, although all samples were exposed for a similar time of ~2 h and under the same stress conditions. The HPMCAS MF combination is therefore found to be relatively stable under the applied humid stress conditions and will need relatively more time to form critical amounts of separated material that has the potential to crystallize. As mentioned and shown in (5e–h), the fracture surfaces of CETP(2) films are characterized by an appearance of small and discrete particles. The density and size of evolved spots vary significantly. Only 5 out of 25 imaged areas have discrete spots on films with PVP VA 64 (Fig. 5e). During the same time, the stressed film surfaces reconstituted with PVP PF 17, PVP K30, and HPMCAS MF exposed spots, islands or new phases over all imaged regions (Fig. 5 f–d). The PVP VA 64 is therefore expected to be more stable than the other combinations. It is the combination expected to need comparatively more time to form a significant amount of separated material, which can then crystallize over time.

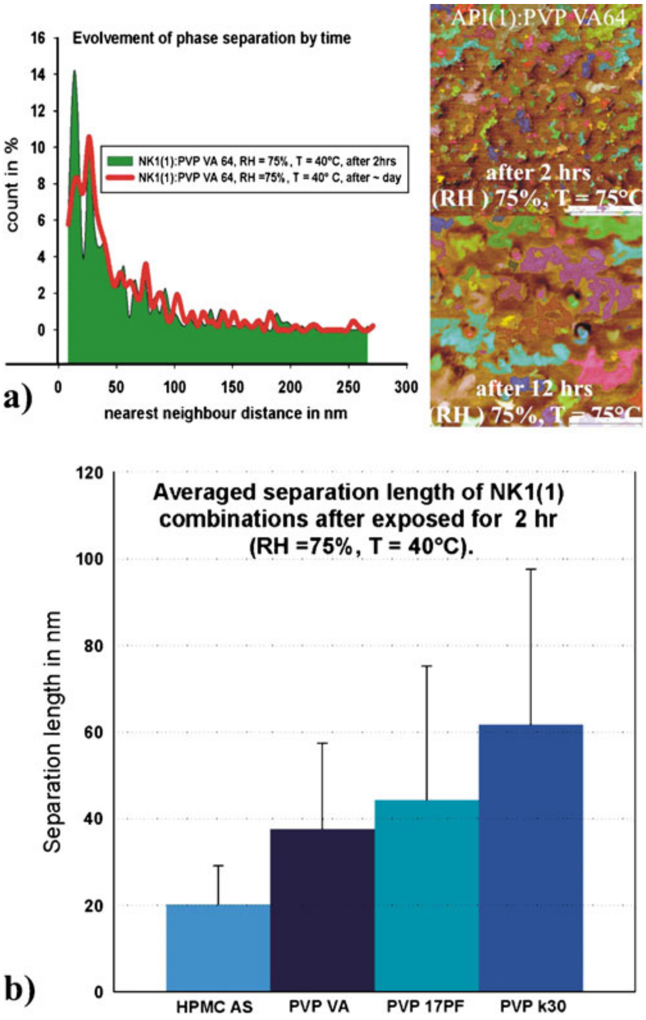

Fig. 6 Phase separation analysis: Histograms in **a** show the nearest neighbor separation of the segregated phases, which characterize fracture surfaces of NK1(1)-PVP VA films after having been exposed to stress conditions (RH=75%, T=40°) for 2 h (green), and after 14 h (red). The corresponding color-coded image analysis data of evolved phases are shown for reference. The *bars* in **b** show the averaged separations and standard deviations of the NK1(1) films after having been stressed for 2 h (RH=75%, T=40°C), for the image data shown in Fig. 5a, b-right, c, d-right.

Figure 7a–d shows humidity-triggered surface de-mixing on a CETP(2): PVP VA 64 film over the course of a week. Exposure to stress conditions first led to a smoothing of the surface; overall, the background remains homogenous. After 2 h, a limited number of about 10 droplets measuring between 50 and 500 nm in diameter are detected on an area measuring 225 μm^2 overall. The general surface coverage at this stage is about 0.2% (Fig. 7b), because just 5 out of 25 imaged places exhibit particles. At this early stage the detected spots have a fluidic shape. After 24 h, 5% of the overall imaged area is locally covered with more regularly-sized particles, which are covered with probably non-crystalline particles (Fig. 7c). Only 12 out of 25 investigated regions are scattered with particles. After a week, star-shaped particles with apparently platelet morphology and ultrathin needles are noticed (Fig. 7d). The overall surface coverage appears, however, not to have dramatically changed. The amount of detected segregates on CETP(2) films with PVP VA 64 is in any case significantly less than the coverage of the other CETP(2) films, where all investigated regions are homogenously covered with segregated material within 2 h.

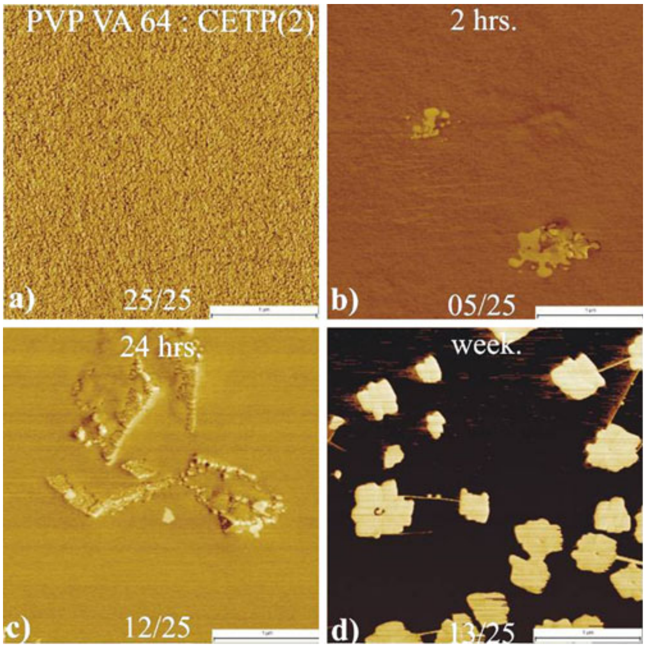

Fig. 7 Phase maps recorded on fracture surface of CETP(2)/PVP VA 64 film initially (**a**), after 2 h (**b**), after 24 h (**c**), and after 1 week (**d**) exposure to stress conditions (RH = 75%, T = 40°C).

Bulk Potential to Undergo Phase Separations with Time and Temperature

To analyze and finally compare the potential of the different combinations to undergo phase separations with time and temperature, the molecular disperse mixtures found within Figs. 2, 3 and 4 were tempered for 96 h, at T= 80°C. After this tempering state, fracture surfaces were created and analyzed by AFM. The bulk potential to phase separate is evaluated by comparing the homogeneity of non-tempered samples (Figs. 3 and 4) with mixtures additionally tempered at T=80°C for 96 h. (Fig. 8). By comparing the bar diagrams of the non-tempered combinations (Fig. 8a/b, left bar sets) with those measured on tempered combinations (Fig. 8a/b, right bar sets), it is evident that bulk de-mixing occurs on some NK1(1) combinations (Fig. 8a). All CETP(2) combinations stay homogenous, as the bar diagrams are quantitatively comparable (Fig. 8b). The phase maps recorded on tempered and non-tempered CETP(2) combinations also only scale with the molecular morphology, like those already shown in the Fig. 4k–o. Figure 8c shows the phase maps of the NK1(1) combinations, where differences are distinct. The corresponding non-tempered data are shown in Fig. 4f–j. Heterogeneity (as per definition introduced previously) is recognizable in the NK1(1) combination with PVP K30, because different regions of the sample clearly vary with respect to their fracture roughness. The roughness variation of different regions is already an order bigger. The PVP K30 phase maps directly show circular-shaped islands, probably fractured droplets, which have diameters in the range of 200 nm (Fig. 8c). The islands or droplets are absent before tempering (shown within Fig. 4f); the combination has phase-separated during treatment.

DISCUSSION

Sample Preparations

To compare the chemical miscibility and stability of different APIs with a set of different excipients melting solvent cast films followed by quench-cooling was found optimal. It is in principle possible to vary API/excipient ratios or to apply various mixing temperatures as, for example, established in high-throughput polymer miscibility screens under use of different optical microscopy techniques, light scattering, or AFM (18,43). The solvent-cast ingredients are likely to be deposited in the form of an amorphous film, which can already be dispersed at the molecular level. Solvent cast films usually need to be intensively dried in high vacuum before being fractured and investigated with for example by AFM (25). This is because many polymers swell with the solvent. The films here are, however, shortly heated to temperature of T= 180°C, which is an intense drying step. The melting points of the investigated APIs are ~40°C below the applied mixing temperature; the obtained liquid melts are free to flow on macroscopic length scales. Possible API grains or crystals, which may have formed during solvent casting, can therefore completely be excluded. In this liquid state the compounds are free to homogenize, or alternatively to form separated phases on the molecular and microscopic scale as shown on the combinations with Eudragit. It should be mentioned that on systems with highly dynamic separating kinetics, the cooling rate has a significant impact on the sample homogeneity achieved and needs to be carefully controlled (44). The cooling rate was kept in the minute range for two reasons: First, such rates better reflect those achieved in production, and, second, the homogeneities achieved and shown within Fig. 4 already meet or are close to the analytical and theoretical limits.

Fractured surfaces have been investigated because heterogeneously structured or less miscible combinations are expected to have the tendency to accumulate or expose only one constituent directly at the surface. These processes are driven by the need to minimize surface tension, and/or they can have physical reasons, as the different physical densities of the involved compounds. We preferred bulk fracture surfaces, because they better reflect the structure and constitution of the origin material than interfaces with, for example, air or glass (26). On poorly miscible polymer mixtures fracturing within a critical temperature range can

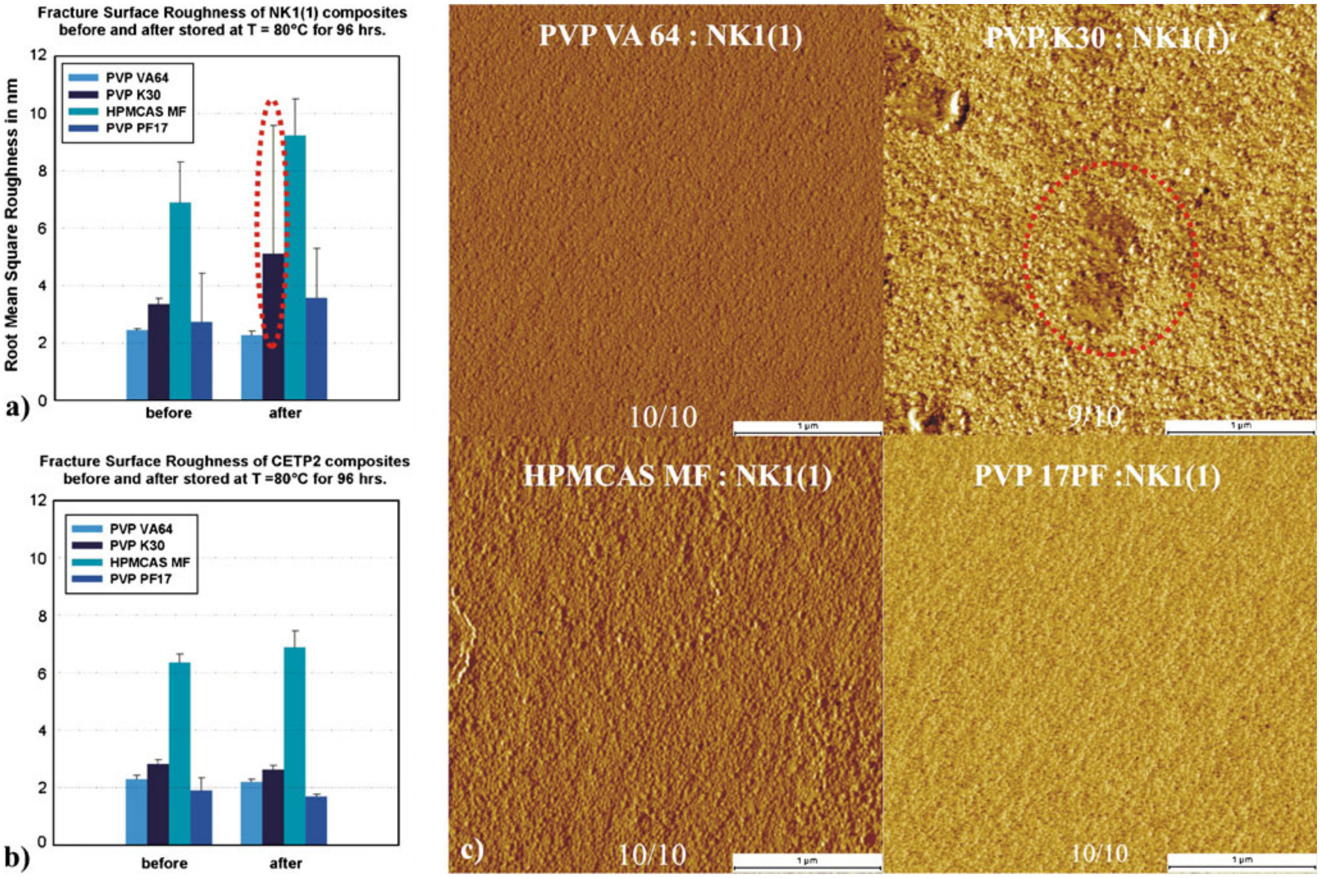

Fig. 8 Homogeneity of NK1(1) and CETP(2) combinations (1:1), which had been stored for 96 h at $T = 80^\circ\mathrm{C}$ before being fractured and characterized. Root Mean Square roughness and sample variations are shown in **a** for the NK1(1) and in **b** for the CETP(2) API/excipient films, before (left) and after (right) tempering at stress conditions. **c** shows $3 \times 3\ \mu\mathrm{m}^2$ sized phase maps of typical appearance for NK1(1) combinations (1:1) after tempering. The phase maps of all CETP(2) combinations are similar with those already shown in Fig. 4k–n.

open an additional kinetic pathway for phase separations. Such mixtures would be excluded from further stability testing, because they are indicated to constitute from not appropriately miscible compounds (45). It needs to be mentioned that all samples here prepared can have microscopic visible defects, often in the form of air bubbles. When the applied temperature is too high, chemical degradations are more likely; the exposure time was therefore chosen short, and the chemical identity controlled with Raman microscopy (Fig. 2).

Homogeneity Criteria

For miscibility, the molecular homogeneity of the different mixtures is probed and compared on different length scales. Microscopic homogeneity is indicated when the API/excipient ratio is found to be nearly constant within a mapping area measuring $240 \times 240\ \mu\mathrm{m}^2$ (Fig. 2). Between 5 and 25 regions on each sample were then additionally investigated with tapping mode AFM. Some of the AFM data presented in Fig. 4 show the probability to find 25 times in a row similarly/comparably structured regions of $3 \times 3\ \mu\mathrm{m}^2$ on a many orders of magnitude larger sample surface. The introduced homogeneity selection criteria are in fact narrow, because the fractured amorphous films are probed for different and independent properties: i) a spectroscopic and microscopic homogenous API/excipient distribution, ii) uniform material fracturing under applied tension on the micrometer and molecular scale, and iii) a molecularly homogenous distribution of the components as visualized within phase contrast maps. The combinations which have a relatively high intrinsic potential to form a single homogenous volume phase are thereby identified, and these can now be proposed for preparation with HME.

Surface Potential to De-mix in Humid Environment

Humidity-triggered phase separations are likely to be surface-directed, because the surface is directly exposed to the humidity, and the bulk is not (46). Phase separation rates measured on the surface generally differ from those of the bulk material. The bulk will de-mix heterogeneously, more gradually, and depending on the correlation length. To quantitatively analyze moisture-induced phase separations with the aim to finally compare material specific rates, and of completely different materials, some basic requirements need to be fulfilled: comparably structured samples and a surface-sensitive tool are required. The applied preparation method and the introduced AFM homogeneity criteria fulfill these needs. The different starting surfaces, i.e., the initial states, are comparable; they only vary with respect to size and structure of the different polymers. The investigated samples are checked for spectroscopic identity and characterized for a defined surface area, their roughness, and molecular homogeneity. The states observed after stress storage can therefore be directly related with the initial surface state. Most other analytical techniques may in daily practice not be able to accurately discriminate between bulk and surface evolution, which can make the direct comparison of different materials difficult.

The spinodal separation patterns observed on mixtures with NK1(1) were analyzed as elsewhere; the different pattern periodicities are characterized and compared (25,26). The dominant wave length observed in Fourier transformed AFM images can be used to quantify pattern periodicity. The concepts work well for an exclusively bi-continuous pattern; the phase map shown in 4b, left panel, is a typical example. It was however noticed that this method can be misleading when the pattern periodicities are narrow and/or range at the molecular morphologic corrugation or the sample roughness. This problem can be avoided by manual fitting of threshold masks to the detected phases and patterns, as explicitly demonstrated in section of Fig. 6a. The features visible are defined as discrete and single particles. The averaged particle separation distance, which is a measure of the pattern periodicity, is then used to compare the differently-sized periodicities of the detected spinodal separation patterns (Figs. 5 and 6b). Principally, it is also possible to compare the size distribution of the separating phase, but such data can then not be directly related to data recorded by, e.g. light scattering. The pattern growth rates in the applied humid conditions are found to increase in the order HPMCAS MF<< PVP VA<PVP17PF<< PVP K30. The observations indicate that the combination with HPMCAS MF can be expected to need relatively more time to form a significant amount of critical-sized domains.

CETP(2) films are found to phase separate as expected for nucleation and growth (21,41). Single islands, which over time can ripen in size, are detected (Fig. 5e–d). The amount of segregated material, which is in the early stage related with the relative surface coverage, is smaller in the composition with PVP VA 64 than in the other compositions. It is indicated that this material needs more time to form a critical amount of CETP(2) domains. It might be mentioned that CETP(2) has a relatively low tendency to crystallize when compared with NK1(1). The AFM observations support this. Nanometer-sized droplets are observed after 2 h of stress storage (Fig. 5), whereas crystals were detected on CETP(2) combinations only after storage for days (Fig. 7).

Bulk Potential to Undergo Phase Separation with Time and Temperature

The bulk potential to de-mix with time and temperature was studied (Fig. 8). The mixtures originally prepared at 180°C before quench-cooling were investigated after an additional tempering storage at 80°C for 96 h at negligible humidity (Fig. 8). The interest is to compare and identify the mixtures where the thermodynamic and/or the kinetic stability are acceptably balanced. The glass transition temperature (Tg) of each system is in fact different, and different scenarios can generally be considered. Some PVP-based mixtures, for example, are known to phase separate up to ~50°C below the Tg (12). We therefore decided to analyze the systems with respect to their tendency to form nanometer-sized separated phases at conditions which are more than 50°C above room temperature. It can be mentioned that identical methods used to analyze humidity-triggered de-mixings can be used to quantify phase separation triggered by temperature; comparably structured and molecularly homogenous initial states need to be stressed. This allows size and amount of separated phases to be compared afterwards. Significant structural change with regard to molecular fracture roughness are noticed on NK1(1) mixtures, except that with PVP VA 64 (Fig. 8a). The observed changes indicate that the NK1(1) combinations do undergo bulk de-mixing and/or structurally change at the applied temperature. Distinct phases in the form of fractured droplets or islands are, however, only noticed in the combination with PVP K30. The CETP(2) combinations, on the other hand, are resistant, because the homogeneity criteria stay quantitatively constant. It can be said that the NK1(1) films appear to have overall more potential to structurally change in the solid state than the CETP(2) films. A likewise stable NK1(1) state is realized with PVP VA 64, which is comparable with the stability of the CETP(2) films.

CONCLUSIONS

An assay has been developed that allows us to access parameters which finally define the long-term stability of a solid dispersion. We demonstrate that the AFM's resolution power allows this to be achieved within hours or days, instead of weeks or months. In the first step of the assay, API/excipient films can be studied with regard to their chemical miscibility. Molecularly disperse combinations can be quantitatively identified. In a second step, the surface potentials to de-mix in a humid environment can be compared. The rates can be determined qualitatively and quantitatively. In a third step, the bulk potential to undergo phase separation can be profiled. Many details, such as the underlying molecular de-mixing mechanisms, mixture-specific separation rates, bulk and surface evolution, are thereby directly visualized. Well-miscible and even stable API:excipient combinations can thus be ranked and be proposed for formulation development.

OUTLOOK

The parameters that are accessible by this novel assay are intrinsic, fundamental, and probably helpful to generally predict the long-term stability of an amorphous formulation. A separate study will be carried out to confirm this hypothesis. Research along this line is in progress.

ACKNOWLEDGEMENTS

The authors would like to thank Natalia Erina, and Chanmin Su for discussions. We would like to thank F. Hoffmann-La Roche Ltd. for the financial support.

REFERENCES

1. Qian F, Huang J, Hussain MA. Drug-polymer solubility and miscibility: stability consideration and practical challenges in amorphous solid dispersion development. J Pharm Sci. 2010;99:2941–7.
2. Flory PJ. Thermodynamics of high polymer solutions. J Chem Phys. 1941;9:660–1.
3. Huggins MM. Thermodynamic properties of solutions of long chain compounds. Ann N Y Acad Sci. 1941;43:1–32.
4. Avraam I. Encyclopedia of Polymer Blends. Wiley-VCH. 1:314 2010.
5. Pajula K, Taskinen M, Lehto VP, Ketolainen J, Korhonen O. Predicting the formation and stability of amorphous small molecule binary mixtures from computationally determined Flory-Huggins interaction parameter and phase diagram. Molecular Pharmaceutics. 2010;7:795–804.
6. Forster A, Hempenstall J, Tucker I, Rades T. Selection of excipients for melt extrusion with two poorly water-soluble drugs by solubility parameter calculation and thermal analysis. Int J Pharm. 2001;226:147–61.
7. Barillaro V, Pescarmona PP, Van Speybroeck M, Do Thi T, Van Humbeeck J, Vermant J, *et al.* High-throughput study of phenytoin solid dispersions: Formulation using an automated solvent casting method, dissolution testing, and scaling-up. J Com Chem. 2008;10:637–43.
8. Van Eerdenbrughand B, Taylor LS. Small scale screening to determine the ability of different polymers to inhibit drug crystallization upon rapid solvent evaporation. Molecular Pharmaceutics. 2010;7:1328–37.
9. Weuts I, Dycke FV, Vorspoels J, De Cort S, Stokbroekx S, Leemans R, *et al.* Physicochemical properties of the amorphous drug, cast films, and spray dried powders to predict formulatiopn probability of success for solid dispersions: etravirine. J Pharm Sci. n/a. (2010), doi:10.1002/jps.22242.
10. Ivanisevic I, Bates S, Chen P. Novel methods for the assessment of miscibility of amorphous drug-polymer dispersions. J Pharm Sci. 2009;98:3373–86.
11. Marsac P, Li T, Taylor L. Estimation of drug-polymer miscibility and solubility in amorphous solid dispersions using experimentally determined interaction parameters. Pharm Res. 2009;26:139–51.
12. Bhattacharya S, Suryanarayanan R. Local mobility in amorphous pharmaceuticals-characterization and implications on stability. J Pharm Sci. 2009;98:2935–53.
13. Rumondor ACF, Stanford LA, Taylor LS. Effects of polymer type and storage relative humidity on the kinetics of felodipine crystallization from amorphous solid dispersions. Pharm Res. 2009;26:2599–606.
14. Rumondor ACF, Marsac PJ, Stanford LA, Taylor LS. Phase behavior of Poly(vinylpyrrolidone) containing amorphous solid dispersions in the presence of moisture. Molecular Pharmaceutics. 2009;6:1492–505.
15. Rumondor ACF, Ivanisevic I, Bates S, Alonzo DE, Taylor LS. Evaluation of drug-polymer miscibility in amorphous solid dispersion systems. Pharm Res. 2009;26:2523–34.
16. Qi S, Belton P, Nollenberger K, Clayden N, Reading M, Craig DQM. Characterisation and prediction of phase separation in hot-melt extruded solid dispersions: a thermal, microscopic and NMR relaxometry study. Pharm Res. 2010;27:1869–83.
17. Janssens S, Van den Mooter G. Review: physical chemistry of solid dispersions. J Pharm Pharmacol. 2009;61:1571–86.
18. Meredith JC, Karim A, Amis EJ. High-throughput measurement of polymer blend phase behavior. Macromolecules. 2000;33:5760–2.
19. Sormana JL, Meredith JC. High-throughput screening of mechanical properties on temperature-gradient polyurethaneurea libraries. Macromol Rapid Commun. 2003;24:118–22.
20. Sawyer LC, Grubb DT, Meyers GF. Polymer microscopy. 3 rd ed. Springer: (2008)
21. Six K, Murphy J, Weuts I, Craig DQM, Verreck G, Peeters J, *et al.* Identification of phase separation in solid dispersions of itraconazole and Eudragit (R) E100 using microthermal analysis. Pharm Res. 2003;20:135–8.
22. Raghavan D, Gu X, VanLandingham M, Nguyen T. Mapping chemically heterogeneous polymer system using selective chemical reaction and tapping mode atomic force microscopy. Macromol Symp. 2001;167:297–305.
23. Wheaton BR, Clare AG. Evaluation of phase separation in glasses with the use of atomic force microscopy. J Non-Cryst Solids. 2007;353:4767–78.
24. Quiroga CC, Bergenstahl B. Characterization of the microstructure of phase segregated amylopectin and beta-lactoglobulin dry mixtures. Food Biophysics. 2007;2:172–82.

25. Cabral JT, Higgins JS, McLeish TCB, Strausser S, Magonov SN. Bulk spinodal decomposition studied by atomic force microscopy and light scattering. Macromolecules. 2001;34:3748–56.
26. Cabral JT, Higgins JS, Yerina NA, Magonov SN. Topography of phase-separated critical and off-critical polymer mixtures. Macromolecules. 2002;35:1941–50.
27. Puri SJ. Surface-directed spinodal decomposition. J Phys Condens Matter. 2005;17:R101–42.
28. Mahlin D, Berggren J, Alderborn G, Engstrom S. Moisture-induced surface crystallization of spray-dried amorphous lactose particles studied by atomic force microscopy. J Pharm Sci. 2004;93:29–37.
29. Mahlin D, Berggren J, Gelius U, Engstrom S, Alderborn G. The influence of PVP incorporation on crystallization rate of amorphous spray-dried lactose powders measured on single particles. J Pharm Pharmacol. 2006;58:A74–5.
30. Ward S, Perkins M, Zhang J, Roberts CJ, Madden CE, Luk SY, *et al.* Novel methods to probe surface amorphous states. J Pharm Pharmacol. 2005;57:S98–8.
31. Ward S, Perkins M, Zhang JX, Roberts CJ, Madden CE, Luk SY, *et al.* Identifying and mapping surface amorphous domains. Pharm Res. 2005;22:1195–202.
32. Price R, Young PM. Visualization of the crystallization of lactose from the amorphous state. J Pharm Sci. 2004;93:155–64.
33. Zhang JX, Bunker M, Chen XY, Parker AP, Patel N, Roberts CJ. Nanoscale thermal analysis of pharmaceutical solid dispersions. Int J Pharm. 2009;380:170–3.
34. Danesh A, Chen X, Davies MC, Roberts CJ, Sanders GHW, Tendler SJB, *et al.* Polymorphic discrimination using atomic force microscopy: distinguishing between two polymorphs of the drug cimetidine. Langmuir. 2000;16:866–70.
35. Tumer YTA, Roberts CJ, Davies MC. Scanning probe microscopy in the field of drug delivery. Adv Drug Deliv Rev. 2007;59:1453–73.
36. Sitterberg J, Ozcetin A, Ehrhardt C, Bakowsky U. Utilising atomic force microscopy for the characterisation of nanoscale drug delivery systems. Eur J Pharm Biopharm. 2010;74:2–13.
37. Conte-Mayweg A, Kuehne H, Luebbers T, Maugeais C, Pflieger P. Indole, indazole or indoline derivatives. US Patent 7259183 (2007).
38. Hoffmann-Emery F, Hilpert H, Scalone M, Waldmeier P. Efficient synthesis of novel NK1 receptor antagonists: selective 1, 4-addition of grignard reagents to 6-chloronicotinic acid derivatives. J Org Chem. 2006;71:2000–8.
39. Mecholsky JJ. Fractal analysis and fractography: what can we learn that's new? Fractography of Advanced Ceramics Iii. 2009;409:145–53. 419.
40. Joseph T, Beatty C, Chen Z, Mecholsky JJ. The use of fractal dimensions to characterize atomic force microscope images of polymer fracture surfaces. Antec'97 Plastics Saving Planet Earth, Conference Proceedings. 1997;13:3371–5. 3801.
41. Sagui C, O'Gorman DS, Grant M. Phase separation: from the initial nucleation stage to the final Ostwald ripening regime. Phase Transformations and Systems Driven Far from Equilibrium. 1998;481:125–30. 686.
42. Henderson IC, Clarke N. On modelling surface directed spinodal decomposition. Macromol Theory Simul. 2005;14:435–43.
43. Meredith JC, Sormana JL, Amis EJ, Karim A, Tona A, Elgendy H. High-throughput characterization of polymer microstructure and mechanical properties. Abstr Pap Am Chem Soc. 2001;222:U327–7.
44. Sakai T, Kamogawa K, Nishiyama K, Sakai H, Abe M. Molecular diffusion of oil/water emulsions in surfactant-free conditions. Langmuir. 2002;18:1985–90.
45. Koyama T, Araki T, Tanaka H. Fracture phase separation. Phys Rev Lett. 102:(2009).
46. Jones RAL, Norton LJ, Kramer EJ, Bates FS, Wiltzius P. Surface-directed spinodal decomposition. Phys Rev Lett. 1991;66:1326–9.